Received: 10 April 2022 | Revised: 4 August 2022 | Accepted: 23 August 2022

DOI: 10.1002/nme.7107

RESEARCH ARTICLE

WILEY

Overcoming volumetric locking in stable node-based smoothed particle finite element method with cubic bubble function and selective integration

Ze-Yu Wang[1,2,3] | **Yin-Fu Jin**[1] | **Zhen-Yu Yin**[2] | **Yu-Ze Wang**[3]

[1]College of Civil and Transportation Engineering, Shenzhen University, Shenzhen, Guangdong, 518060, China

[2]Department of Civil and Environmental Engineering, The Hong Kong Polytechnic University, Kowloon, China

[3]Department of Ocean Science and Engineering, Southern University of Science and Technology, Shenzhen, China

Correspondence
Yin-Fu Jin, College of Civil and Transportation Engineering, Shenzhen University, Shenzhen 518060, Guangdong, China.
Email: yinfu.jin9019@gmail.com
Zhen-Yu Yin, Department of Civil and Environmental Engineering, The Hong Kong Polytechnic University, Hung Hom, Kowloon, Hong Kong, China.
Email: zhenyu.yin@polyu.edu.hk

Funding information
Research Grants Council (RGC) of Hong Kong Special Administrative Region Government (HKSARG) of China, Grant/Award Number: R5037-18F; Project of Research Institute of Land and Space (CD78); Hong Kong Polytechnic University Strategic Importance Fund (ZE2T)

Abstract

The stable node-based smoothed particle finite element method (SNS-PFEM) reduces spatial numerical oscillation from direct nodal integration in NS-PFEM but leads to a severe volumetric locking effect when modeling nearly incompressible materials-related boundary value problems. This study proposes an improved locking-free SNS-PFEM to investigate the performance of the bubble function and selective integration scheme in circumventing volumetric locking. Three locking-free variants of SNS-PFEM: (1) SNS-PFEM with a cubic bubble function (bSNS-PFEM), (2) SNS-PFEM with a selective integration scheme (selective SNS-PFEM), and (3) SNS-PFEM with a cubic bubble function and selective integration scheme (selective bSNS-PFEM)—were gradually developed for comparison. The performance of these three approaches was first successively examined using two examples with elastic materials, that is, an infinite plate with a circular hole and Cook's membrane. The comparisons show that the cubic bubble function and selective integration scheme are both necessary as a locking-free approach for modeling nearly incompressible materials, and the proposed selective bSNS-PFEM performs best among the three variants in terms of accuracy and convergence. Two examples of slope stability analysis and footing penetration on elastoplastic materials were then conducted by SNS-PFEM and the proposed selective bSNS-PFEM. The results indicate that the proposed selective bSNS-PFEM is stable and accurate, even when accompanied by significant deformation. All obtained results indicate that the locking-free selective bSNS-PFEM is a powerful approach for modeling nearly incompressible materials with both material and geometric nonlinearity.

KEYWORDS

bubble function, NS-PFEM, selective integration scheme, stable nodal integration, volumetric locking

1 | INTRODUCTION

Soft clays are usually considered nearly incompressible under undrained analysis, and their behaviors can be approximately simulated using a pure cohesive constitutive model with a Poisson's ratio approaching 0.5. The engineering

problems involving nearly incompressible clays, such as the bearing capacity of foundation in soft clay, the progressive failure of slope in structured soft clay and the pipeline penetrating the soft clay, always show the characteristics of large deformation. Therefore, to solve such problems, a reliable locking-free numerical method with the ability to simulate large deformation is required.

The particle finite element method (PFEM), which is based on an updated Lagrangian framework, has been widely used for large deformation simulation in geotechnical engineering.[1–6] In engineering practice, the PFEM with low-order elements (e.g., 3-node linear triangular element, T3) is advantageous. The numerical implementation is simpler due to the same shape functions for all variables. It is also flexible in the adaptive re-mesh process using Delaunay triangulation. However, such methods with low-order elements are susceptible to volumetric locking when modeling a nearly incompressible solid, which is characterized by an "overly-stiff" solution with a spurious checkerboard distribution of stress and strain.[7–10] This issue especially plagues low-order PFEMs with multiple quadrature points, since excessive constraints are imposed on the deformation of elements, violating the divergence-free condition of interpolated displacement.[11–13]

The strain smoothing technique is an effective way to improve the performance of PFEM with low-order elements,[14] such as the node-based smoothed PFEM (NS-PFEM)[15–19] and edge-based smoothed PFEM (ES-PFEM).[20,21] S-PFEMs are famous for their potential to reduce—although not necessarily eliminate—volumetric locking.[11,22] Besides, S-PFEMs are more robust with mesh distortion and achieve better accuracy in strain energy than that of traditional PFEM.[11,23,24] NS-PFEM is relatively superior to ES-PFEM in the re-meshing procedure because all the physical quantities are stored based on nodes, then the variable mapping between nodes and quadrature points is avoided, which used to be a prominent source of accuracy loss in traditional PFEM or ES-PFEM.[21,25,26] However, NS-PFEM with direct nodal integration (NI) has its defects in detecting "overly-soft" properties[27,28] and spatial instability due to the spurious low-energy mode of NI.[29,30] To solve the aforementioned problems of NI, several stable nodal integration (SNI) techniques have been proposed and implemented into NS-PFEM, leading to a novel framework called stable node-based smoothed PFEM (SNS-PFEM).[27,31] SNI relies on adding more evaluation points in subdomains using implicit strain gradients or subdomain-smoothed gradients.[22,27,32–35] However, the combination of PFEM with low-order elements with additional quadrature points will likely further weaken its locking-free ability.[7–10]

To solve volumetric locking, a variety of techniques have been proposed for traditional FEM S-FEM and meshfree methods, including *u-p* two field mixed formulations,[13,36] the B-bar and F-Bar methods,[7,9,10,37–39] selective reduced integration,[9,12,40] enhanced assumed strain element,[41,42] mixed variational methods,[43] the bubble function method,[11,44,45] and volume-averaged nodal projection techniques.[8] However, such approaches have not been adopted to solve the volumetric locking problem of SNS-PFEM. Therefore, the performance of such locking-free methods in SNS-PFEM is worth investigating.

This study aims to propose a locking-free SNS-PFEM for nearly incompressible materials. This article is outlined as follows. Sections 2.1 and 2.2 detail the FEM formulations for quasi-static solids based on the 3-node triangular mesh. Section 2.3 presents the framework of node-based smoothed particle FEM with stable nodal integration. Section 2.4 demonstrates the cause of the volumetric locking effect of SNS-PFEM. Section 3 presents several novel treatments of volumetric locking for SNS-PFEM, namely, the cubic bubble function, selective integration scheme, and hybrid strategy. In Section 4, a wide range of examples concerning nearly incompressible solids are simulated with several numerical formulations based on SNS-PFEM. The performance of these formulations in curing volumetric locking is thoroughly evaluated. Finally, conclusions are drawn in Section 5.

2 | BRIEF INTRODUCTION OF SNS-PFEM

2.1 | Governing equations

The equilibrium equation for a continuous solid is expressed as Equation (1). The linear geometric relationship between strain $\boldsymbol{\varepsilon}$ and displacement $\mathbf{u}$ is formulated by the symmetrical gradient operator ∇^s in Equation (2). The constitutive equation could be written as a rate-dependent formulation as shown in Equation (3). The imposed and natural boundary conditions Γ_u and Γ_t, respectively, are presented in Equation (4),

$$\nabla \cdot \boldsymbol{\sigma} + \mathbf{b} = \mathbf{0}, \tag{1}$$

$$\boldsymbol{\varepsilon} = \nabla^s \mathbf{u} = \frac{1}{2}\left(\nabla \mathbf{u} + \nabla \mathbf{u}^T\right), \tag{2}$$

$$\frac{d}{dt}\boldsymbol{\sigma} = \mathbb{D}_{ep} : \frac{d}{dt}\boldsymbol{\varepsilon}, \tag{3}$$

$$\begin{cases} \mathbf{u} = \overline{\mathbf{u}} \text{ on } \Gamma_u \\ \mathbf{n}\cdot\boldsymbol{\sigma} = \bar{\mathbf{t}} \text{ on } \Gamma_t \end{cases}, \text{where } \Gamma = \Gamma_u \cup \Gamma_t, \ \ \Gamma_u \cap \Gamma_t = \emptyset, \tag{4}$$

where $\boldsymbol{\sigma}$ is the Cauchy stress tensor, $\mathbf{b}$ the body force, $\mathbb{D}_{ep}$ the fourth-order algorithm modulus tensor, $\overline{\mathbf{u}}$ the given displacement, and $\bar{\mathbf{t}}$ the imposed traction force.

2.2 | Weak form and spatial discretization

The above governing PDEs with boundary conditions could be reformulated as an equivalent weak form in Equation (5) using the virtual displacement principle and integration by parts. The displacement $\mathbf{u}$ and its variation $\delta\mathbf{u}$ are defined in adequate trial function space S_u and test function spaces V_u separately.

$$\int_\Omega \nabla^s \delta\mathbf{u} : \boldsymbol{\sigma} d\Omega = \int_\Omega \delta\mathbf{u}\cdot\mathbf{b} d\Omega + \int_{\Gamma_t} \delta\mathbf{u}\cdot\bar{\mathbf{t}} d\Gamma. \tag{5}$$

Interpolated displacement $\mathbf{u}^h$ by spatial discretisation takes the form of linear combinations of nodal shape functions, as shown in Equation (6):

$$\mathbf{u}^h = \mathbf{N}\mathbf{U}, \tag{6}$$

where $\mathbf{N}$ is the global shape function matrix and $\mathbf{U}$ the array of nodal displacement. The interpolation with linear triangulation element (T3) is adopted in this study.

The FEM equation in matrix form is then formulated as the balance of internal force $\mathbf{F}^{int}$ and external force $\mathbf{F}^{ext}$ in Equations (7)–(10). The compatible $\mathbf{B}$ matrix in Equation (8) is calculated by the displacement gradient operator $\mathbf{L}_d$.

$$\mathbf{F}^{int} = \mathbf{F}^{ext}, \tag{7}$$

$$\mathbf{F}^{int} = \int_\Omega \mathbf{B}^T\boldsymbol{\sigma} d\Omega, \mathbf{B} = \mathbf{L}_d\mathbf{N}, \tag{8}$$

$$\mathbf{F}^{ext} = \int_{\Gamma_t} \mathbf{N}^T\bar{\mathbf{t}} d\Gamma + \int_\Omega \mathbf{N}^T\mathbf{b} d\Omega, \tag{9}$$

$$\mathbf{K} = \int_\Omega \mathbf{B}^T\mathbf{D}\mathbf{B} d\Omega. \tag{10}$$

2.3 | NS-PFEM with stable nodal integration (SNS-PFEM)

In NS-PFEM, the compatible strain $\boldsymbol{\varepsilon}$ and gradient matrix $\mathbf{B}$ are converted into their smoothed counterparts $\overline{\boldsymbol{\varepsilon}}$ and $\overline{\mathbf{B}}$ based on the gradient smoothing operator $\overline{\nabla}$. The first step is constructing the node-based smoothing domain Ω_k^s with subdomains $\Omega_{k,q}^s$ in a triangular mesh, as depicted in Figure 1, where the coordinate of node I is marked as $\mathbf{x}_k$. The vertices of Ω_k^s are composed of the centroids of adjacent elements and the midpoints of the connected edges. The gradient smoothing operator $\overline{\nabla}$ takes the weighted integration of the compatible gradient over the whole domain with a piecewise-constant and compactly-supported weight function, as shown in Equations (11) and (12). Then the stiffness matrix assembly and internal force calculation are conducted by nodal integration. NS-PFEM utilizes the information propagated from more adjacent elements, which is anticipated to be more accurate than traditional FEM-T3 in the strain energy norm.[11,23,28] The formulations of calculating smoothed gradient matrix $\overline{\mathbf{B}}$ with numerical integration are exhibited in Appendix A.

$$\overline{\nabla} N(\mathbf{x})|_{\Omega_k^s} = \int_{\Omega_k^s} \nabla N(\mathbf{x}) W(\mathbf{x}_k - \mathbf{x}) d\mathbf{x}, \text{where } W(\mathbf{x}_k - \mathbf{x}) = \begin{cases} 1/A_k^s, \mathbf{x} \in \overline{\Omega}_k^s. \\ 0, \mathbf{x} \notin \overline{\Omega}_k^s, \end{cases} \tag{11}$$

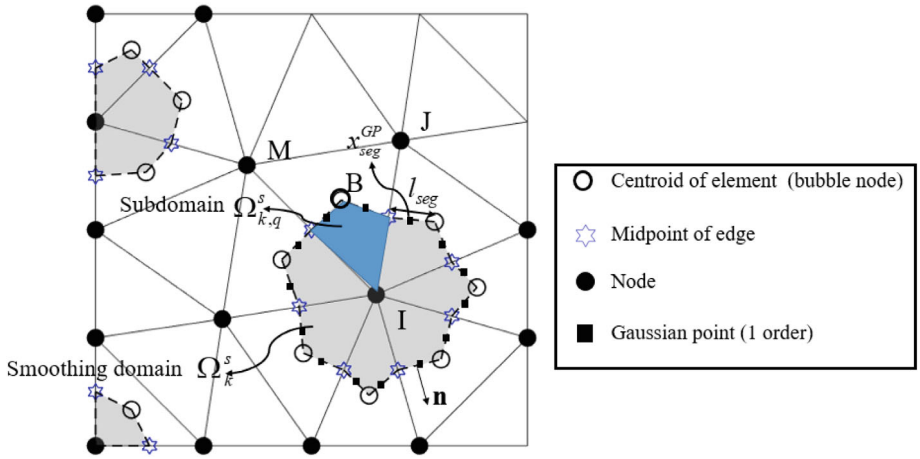

FIGURE 1 Schematic of the node-based smoothing domain with T3 mesh and internal bubble node

$$\bar{\boldsymbol{\varepsilon}}(\mathbf{x})|_{\Omega_k^s} = \frac{1}{A_k^s}\int_{\Omega_k^s} \boldsymbol{\varepsilon}(\mathbf{x})d\Omega. \tag{12}$$

The integration of a smoothed stiffness matrix might be conducted in direct nodal integration (NI) based on the smoothing domain, as shown in Equation (13). However, the direct nodal integration used for solving the smoothed Galerkin weak form could introduce the loss of coercivity in the limit of mesh refinement, and such numerical instability will lead to the spurious saw tooth mode.[29,34,46] The modified SNI method proposed by Chen et al.[29,34,46] could cure this problem, as it uses the difference between the smoothed $\overline{\mathbf{B}}$ and the subdomain-smoothed $\overline{\mathbf{B}}^{sub}$ matrix, as shown in Equation (14). For linear triangular element, the subdomain-smoothed $\overline{\mathbf{B}}^{sub}$ matrix takes the same value of the compatible $\mathbf{B}$ matrix. For higher-order interpolation, they are not equal. Noticing that the smoothed $\overline{\mathbf{B}}$ matrix is constant in the smooth domain, and the subdomain-smoothed $\overline{\mathbf{B}}^{sub}$ matrix is also constant in the subdomain. Thus, the integration of Equations (13) and (14) can be simply performed by the superposition of multiplication of a constant matrix with the area of subdomain. By implementing SNI into NS-PFEM, a novel framework called SNS-PFEM is achieved.

$$\left[\overline{\mathbf{K}}_{IJ}\right]_{\Omega_k^s} = \int_{\Omega_k^s} \overline{\mathbf{B}}_I^T \mathbf{D}\overline{\mathbf{B}}_J d\mathbf{x}, \tag{13}$$

$$\left[\overline{\mathbf{K}}_{IJ}\right]_{\Omega_k^s} = \int_{\Omega_k^s} \overline{\mathbf{B}}_I^T \mathbf{D}\overline{\mathbf{B}}_J d\mathbf{x} + \sum_{q=1}^{n_k}\int_{\Omega_{k,q}^s} \left(\overline{\mathbf{B}}_I - \overline{\mathbf{B}}^{sub}{}_{I,q}\right)^T \mathbf{D}\left(\overline{\mathbf{B}}_J - \overline{\mathbf{B}}^{sub}{}_{J,q}\right) d\mathbf{x},$$

$$\text{with } \overline{\mathbf{B}}^{sub}{}_{I,q}\Big|_{\Omega_{k,q}^s} = \frac{1}{A_{k,q}^s}\int_{\Omega_{k,q}^s} \mathbf{B}_I d\Omega. \tag{14}$$

The SNS-PFEM adopts the re-meshing strategy using Delaunay triangulation and the alpha shape algorithm to conduct a large deformation analysis.[16,26,27] The nodes are regarded as a moving particle cloud for domain discretisation with the variables of interest frequently updated as the configuration varies. The node-based smoothing framework is especially suitable for a particle method because all physical quantities of interest are stored at nodes (i.e., displacements) or updated by the node-based smoothing domains (i.e., strain, stress, state variables of the soil model) and the variable mapping between the nodes and quadrature points are no longer needed, resulting in less information loss and higher efficiency.[27] Since the total variation of geometry would be decomposed into many small steps, the accuracy of the infinitesimal strain geometric equation could still be guaranteed, as demonstrated in previous studies.[5,6,19] The computational cycle of SNS-PFEM is exhibited in Appendix B.

2.4 | Volumetric locking of SNS-PFEM

When simulating incompressible or nearly incompressible solids, the extra physical constraint of no volumetric strain must be satisfied. The discretized scheme poses a divergence-free condition to interpolated displacement, as

shown in Equation (15):

$$\nabla \cdot \mathbf{u}^h \to 0 \text{ as } \upsilon \to 0.5, \tag{15}$$

where υ is Poisson's ratio.

When low-order elements with full integration are used, this divergence-free condition is difficult to conform under a nearly incompressible limit, leading to an overly stiff response with a checkboard distribution of stress. This phenomenon is called the "volumetric locking effect." Intuitive insight can be given to the FEM-T3. The gradients of the T3 shape function have some constants determined by the geometry of each element, so each evaluation of the constitutive model at a quadrature point introduces a linear correlation constraint to the nodal displacements. Consequently, redundant constraints will lead to spurious solutions dominated by the element's geometry, which is characterized by overly small displacement and an unusual stress distribution. According to References 12,47, the ratio r of the unknown degrees of freedom (DOF) over incompressible constraints can be used to evaluate the extent of volumetric locking, as shown in Equation (16):

$$r = \frac{n_{eq}}{n_c}, \tag{16}$$

where n_{eq} is the total number of unknown nodal displacement equations to be solved, and n_c is the total number of incompressible constraints. According to Hughes,[12] $r = 2$ offers the optimal performance in 2D incompressible problems, which indicates that the number of equilibrium equations divided by the number of incompressible conditions equals the dimension of space. As r decreases, the tendency toward lock would appear. When $r < 1$, there are more volumetric deformation constraints than displacement degrees of freedom available and severe locking can thus be anticipated.

In NS-PFEM, each interior node carries 2 unknown displacement components in the 2D problem, while each interior or boundary node poses 1 constraint from the evaluation of strain and stress. When the mesh is very fine, the number of fixed DOFs due to the given boundary conditions can be neglected compared to the total number of DOFs, making the ratio r approach the optimal value 2, which makes NS-PFEM locking-free. For coarse mesh, the ratio r is smaller than 2 and the locking effect becomes prominent, which has been supported by an eigenvalue analysis.[47]

However, SNS-PFEM recovers the gradient distribution of smoothed strain and introduces additional constraints to the deformation of the element. The evaluation of the subdomain-smoothed gradient is equal to introducing extra quadrature points in each subdomain, which dramatically increases n_c and decreases the ratio r to a value lower than 1. Then volumetric locking can be anticipated to be much more severe than that of NS-PFEM. In the following sections, this phenomenon will be highlighted by several numerical examples.

3 | VOLUMETRIC-LOCKING-FREE SNS-PFEM

3.1 | Interpolation space enriched by cubic bubble function

In this study, several attempts are considered to circumvent the volumetric locking effect of SNS-PFEM. First, injecting extra flexibility into the interpolated space could achieve some softening effect, which may help when the strain smoothing operator is applied in a displacement-driven framework.[11] Here the idea is implemented by equipping each element with an internal node at the centroid of the element,[11,44,45] as exhibited in Figures 1 and 2A. This approach, n_{eq} undergoes a massive increase, but n_c shows no change, enhancing the ratio r in Equation (16) and then lowering the tendency toward element locking. The bubble nodes can be automatically located in a T3 mesh so that no extra division of the element patch needs to be constructed compared with that of the generalized F-Bar or B-Bar techniques.[10,37]

The shape function of each internal node, called the bubble function, is compactly supported only by the single element where the node is located. The cubic bubble function N_B^b marked by the internal node B equals the product of three vertex shape functions N_I, N_J, N_M scaled by a factor of 27, as shown in Equation (17), which takes the maximum value 1 at the centroid and the minimum 0 on three edges, as illustrated in Figure 2B. Unlike the MINI element which requires u-p FEM formulation,[45] here a pure displacement-based framework is preserved. Only the displacement $\mathbf{u}$ is interpolated in the enriched interpolated space, which has been proved effective in ES-FEM.[11] Thus, plugging the bubble function into

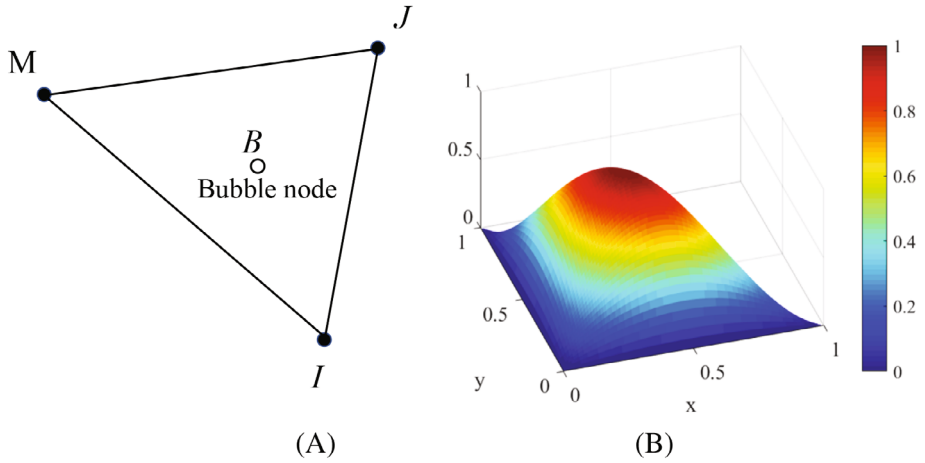

FIGURE 2 (A) 3-node triangular element with a bubble node and (B) image of the cubic bubble function

the original displacement-driven S-PFEM code is straightforward and without any fundamental modifications.

$$N_B^b(\mathbf{x}) = 27 N_I N_J N_M. \tag{17}$$

With internal bubble nodes, the whole shape function matrix in Equation (18) can be divided into two distinct groups: the linear shape function of vertex nodes $\mathbf{N}_{Tri}$ and the cubic bubble shape function of internal nodes $\mathbf{N}_{Bub}$. The nodal displacement and smoothed gradient matrix are also grouped in the same manner, as shown in Equations (19) and (20). It is worth emphasizing that this division is only a conceptual expression rather than a record of the real data structure in the codes. It may be more computationally efficient to number the degrees of freedom element by element when considering the stiffness matrix bandwidth.

$$\mathbf{N} = [\mathbf{N}_{Tri} \;\; \mathbf{N}_{Bub}] = \left[\mathbf{N}_1 \quad \dots \quad \mathbf{N}_{n_d} \quad \mathbf{N}_1^b \quad \dots \quad \mathbf{N}_{n_e}^b\right], \tag{18}$$

$$\mathbf{U} = \begin{bmatrix} \mathbf{U}_{Tri} \\ \mathbf{U}_{Bub} \end{bmatrix}, \tag{19}$$

$$\overline{\mathbf{B}} = \overline{\mathbf{L}}_d \mathbf{N} = \left[\overline{\mathbf{B}}_1 \quad \dots \quad \overline{\mathbf{B}}_{n_d} \quad \overline{\mathbf{B}}_1^b \quad \dots \quad \overline{\mathbf{B}}_{n_e}^b\right]. \tag{20}$$

The interpolated trial function space S_u^h and test function space V_u^h enriched by the cubic bubble function are exhibited in Equations (21) and (22). The approximated displacement restricted on a single element $\mathbf{u}^h(\mathbf{x})\big|_{\Omega_e}$ is expressed as shown in Equation (23).

$$S_u^h = \left\{ \mathbf{u}^h : \Omega \to R^d | \mathbf{u}^h = \mathbf{N}\mathbf{W} \text{ with } \mathbf{W} \in \mathbf{R}^{(d\cdot n_d + d\cdot n_e)\times 1}, \mathbf{u}^h = \overline{\mathbf{u}} \text{ on } \Gamma_u \right\}, \tag{21}$$

$$V_u^h = \left\{ \delta\mathbf{u}^h : \Omega \to R^d | \delta\mathbf{u}^h = \mathbf{N}\mathbf{V} \text{ with } \mathbf{V} \in \mathbf{R}^{(d\cdot n_d + d\cdot n_e)\times 1}, \delta\mathbf{u}^h = \mathbf{0} \text{ on } \Gamma_u \right\}, \tag{22}$$

$$\mathbf{u}^h(\mathbf{x})\Big|_{\Omega_e} = \sum_{i\in\{I,J,M\}} \begin{bmatrix} N_i(\mathbf{x}) & 0 \\ 0 & N_i(\mathbf{x}) \end{bmatrix} \begin{bmatrix} U_{ix} \\ U_{iy} \end{bmatrix} + \begin{bmatrix} N_B^b(\mathbf{x}) & 0 \\ 0 & N_B^b(\mathbf{x}) \end{bmatrix} \begin{bmatrix} U_{Bx}^b \\ U_{By}^b \end{bmatrix}. \tag{23}$$

Thus, introducing the bubble nodes into the T3 elements, a variant SNS-PFEM aimed at easing the locking with bubble elements is proposed and marked as "bSNS-PFEM" in this study.

3.2 | Selective integration scheme

The selective integration scheme which decomposes the modulus tensor and treats the volumetric and deviatoric parts separately has been widely adopted in S-FEMs to solve the volumetric locking problem when simulating nearly

incompressible materials.[22,24,40] It is regarded as a simple fix when the locking effect is not extremely severe. The elastic modulus $\mathbf{D}_e$ is often decomposed into the shearing part $\mathbf{D}_\mu$ and volumetric part $\mathbf{D}_\lambda$ as formulated in Equation (24), where μ is the shearing modulus $\mu = E/2(1+\upsilon)$ and λ is the Lame's parameter $\lambda = \upsilon E/(1+\upsilon)(1-2\upsilon)$. The initial elastic stiffness matrix could also be split into volumetric and shearing components, as shown in Equation (25).

$$\mathbf{D}_e = \mu \begin{bmatrix} 2 & 0 & 0 \\ 0 & 2 & 0 \\ 0 & 0 & 1 \end{bmatrix} + \lambda \begin{bmatrix} 1 & 1 & 0 \\ 1 & 1 & 0 \\ 0 & 0 & 0 \end{bmatrix} = \mathbf{D}_\mu + \mathbf{D}_\lambda, \tag{24}$$

$$\mathbf{K}_e = \int_\Omega \mathbf{B}^T \mathbf{D}_e \mathbf{B} d\Omega = \int_\Omega \mathbf{B}^T \mathbf{D}_\mu \mathbf{B} d\Omega + \int_\Omega \mathbf{B}^T \mathbf{D}_\lambda \mathbf{B} d\Omega. \tag{25}$$

A selective integration scheme with the decomposition of the elastic modulus (selective SNI) in Equation (24) is exhibited here.[22] When treating nearly incompressible solids, only the shearing part $\mathbf{D}_\mu$ is adopted in the stabilization terms, while the whole $\mathbf{D}$ is still preserved in main stiffness integration, as shown in Equation (26). Therefore, the additional constraint on volumetric deformation from stabilization is excluded, while integration stabilization still plays its role.

$$\left[\overline{\mathbf{K}}_{IJ}\right]_{\Omega_k^s} = \int_{\Omega_k^s} \overline{\mathbf{B}}_I^T \mathbf{D} \overline{\mathbf{B}}_J d\mathbf{x} + \sum_{q=1}^{n_k} \int_{\Omega_{k,q}^s} \left(\overline{\mathbf{B}}_I - \overline{\mathbf{B}}_{J,q}^{sub}\right)^T \mathbf{D}_\mu \left(\overline{\mathbf{B}}_J - \overline{\mathbf{B}}_{J,q}^{sub}\right) d\mathbf{x}. \tag{26}$$

Thus, adopting selective integration, the other locking-free variant SNS-PFEM with selective integration is proposed and marked as "Selective SNS-PFEM" in this study.

Furthermore, the selective integration scheme can also be used in bSNS-PFEM, producing a hybrid locking-free variant of SNS-PFEM called "Selective bSNS-PFEM". Three locking-free variants of SNS-PFEM will be examined in the following sections.

4 | NUMERICAL EXAMPLES

In this section, four problems involving nearly incompressible materials are simulated by some of the three locking-free variants of SNS-PFEM (i.e., bSNS-PFEM, Selective SNS-PFEM and Selective bSNS-PFEM). The same cases are also simulated using NS-PFEM and SNS-PFEM for comparison. Two homogenous linear elastic cases are simulated first, namely, an infinite plate with a circular hole and Cook's membrane. Then the slope stability analysis on both Tresca and Mohr-Coulomb (MC) soil is conducted. Finally, the example of strip footing on Tresca soil is simulated for both small and large deformation.

4.1 | Infinite plate with a circular hole

To examine the convergence and accuracy of the above numerical formulations in nearly incompressible conditions, an infinite elastic plate with a circular hole subjected to uniaxial tension in the x-direction is analyzed.[24,27] A quarter of the geometry with a side length of $b = 5$ m is taken due to symmetry, and roller boundary conditions are imposed, as shown in Figure 3.

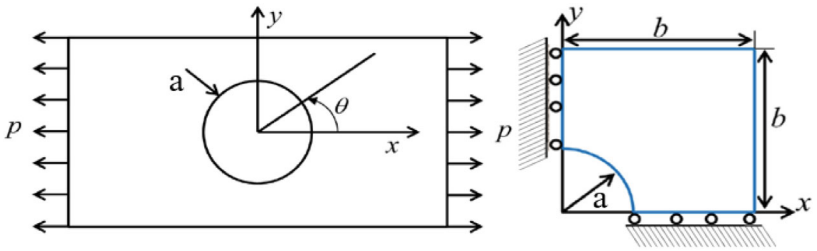

FIGURE 3 An infinite plate with a circular hole subjected to uniaxial tension

The hole radius is $a = 1$ m. The tension on the infinite boundary is 1 N/m. Young's modulus $E = 1$ kPa and a sequence of Poisson's ratios approaching 0.5 (υ from 0.25 to 0.4999999 in this case) are adopted. Analytical solutions for displacement and stress are available in Equations (27) and (28), where r and θ are polar coordinates, and two material parameters can be acquired by $\mu = \epsilon/2(1+\upsilon)$ and $\kappa = 3-4\upsilon$. The traction boundary conditions are then imposed directly from the analytical stress distribution. T3 mesh with 881 nodes and 1628 elements is then generated.

$$\begin{cases} \sigma_{xx} = 1 - \frac{a^2}{r^2}\left[\frac{3}{2}\cos 2\theta + \cos 4\theta\right] + \frac{3a^4}{2r^4}\cos 4\theta, \\ \sigma_{yy} = \frac{a^2}{r^2}\left[\frac{1}{2}\cos 2\theta - \cos 4\theta\right] - \frac{3a^4}{2r^4}\cos 4\theta, \\ \tau_{xy} = -\frac{a^2}{r^2}\left[\frac{1}{2}\sin 2\theta + \sin 4\theta\right] + \frac{3a^4}{2r^4}\sin 4\theta, \end{cases} \tag{27}$$

$$\begin{cases} u_x = \frac{a}{8\mu}\left[\frac{r}{a}(\kappa+1)\cos\theta + 2\frac{a}{r}((1+\kappa)\cos\theta + \cos 3\theta) - 2\frac{a^3}{r^3}\cos 3\theta\right], \\ u_y = \frac{a}{8\mu}\left[\frac{r}{a}(\kappa-1)\sin\theta + 2\frac{a}{r}((1-\kappa)\sin\theta + \sin 3\theta) - 2\frac{a^3}{r^3}\sin 3\theta\right]. \end{cases} \tag{28}$$

To evaluate the accuracy of the numerical results, the L_2 displacement error norm E_d[11] is defined as in Equation (29):

$$E_d = \left(\int_\Omega \left(\mathbf{u} - \mathbf{u}^h\right)^T \left(\mathbf{u} - \mathbf{u}^h\right) d\Omega\right)^{1/2}, \tag{29}$$

where $\mathbf{u}^h$ is the interpolated displacement in Equation (6), and $\mathbf{u}$ is the analytical solution.

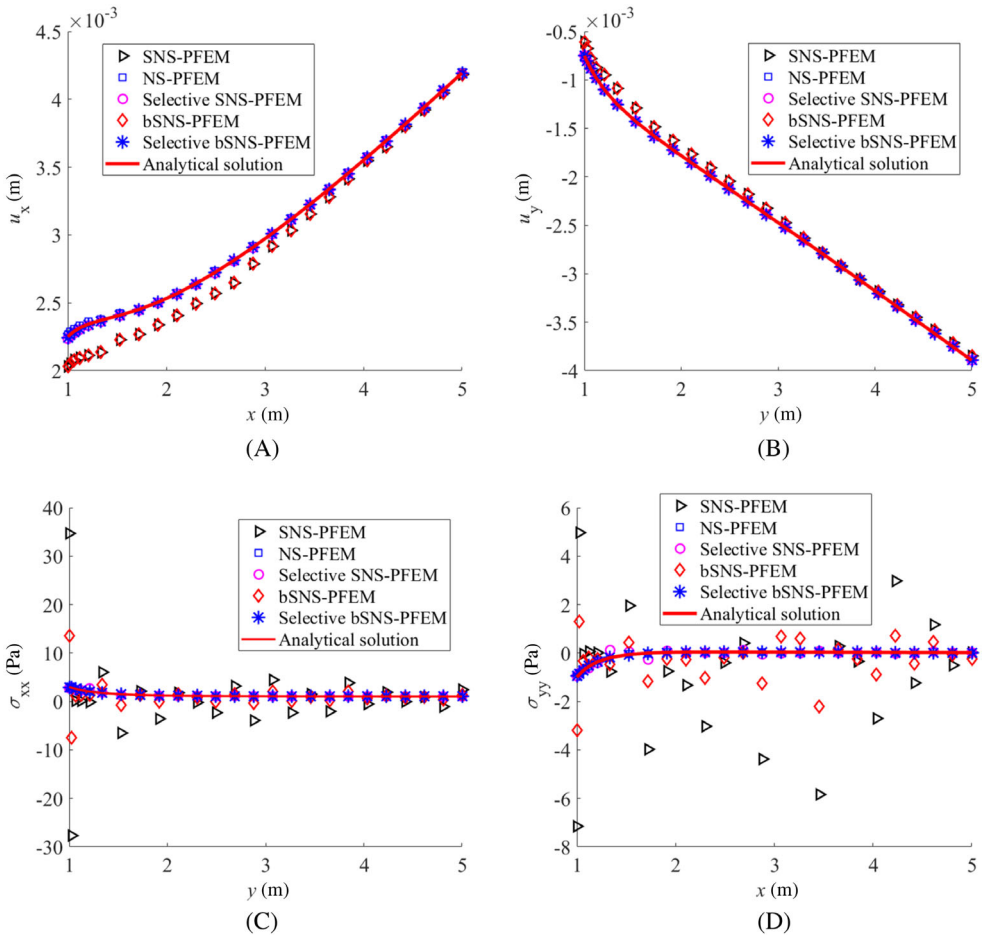

FIGURE 4 Distribution of (A) displacement along the bottom boundary; (B) displacement along the left boundary; (C) normal stress along the left boundary; (D) normal stress along the bottom boundary, of the infinite plate with a circular hole subjected to uniaxial tension ($\upsilon = 0.4999999$)

Figure 4 presents the displacement and normal stress distribution along the left and bottom edge from numerical and analytical approaches. It seems that only the SNS-PFEM and bSNS-PFEM generate biased displacement and severely oscillatory stress along boundaries. From the contour of the vertical normal stress in Figure 5, the global performance of numerical stability can be observed. The result of SNS-PFEM presents a typical checkboard pattern due to volumetric locking, which can be slightly eased by the bubble function or selective stable integration, as shown in Figure 5C,D, but not by much. Conversely, NS-PFEM provides a near non-locking mode, but the contour is saw-toothed because of the spurious zero-energy mode of direct nodal integration. A globally smooth distribution can be acquired by the hybrid strategy, as shown in Figure 5E, which combines the bubble function with selective stable integration.

The curves of displacement error norm versus a sequence of Poisson's ratios approaching 0.5 shown in Figure 6 give a more accurate evaluation of their locking-free ability. The error of NS-PFEM almost does not vary with Poisson's ratio in the incompressible limit, although it is never the lowest due to the accuracy loss from NI. The error of SNS-PFEM increases significantly when the Poisson's ratio exceeds 0.49, then tends to be stable from around 0.49999. Adding the

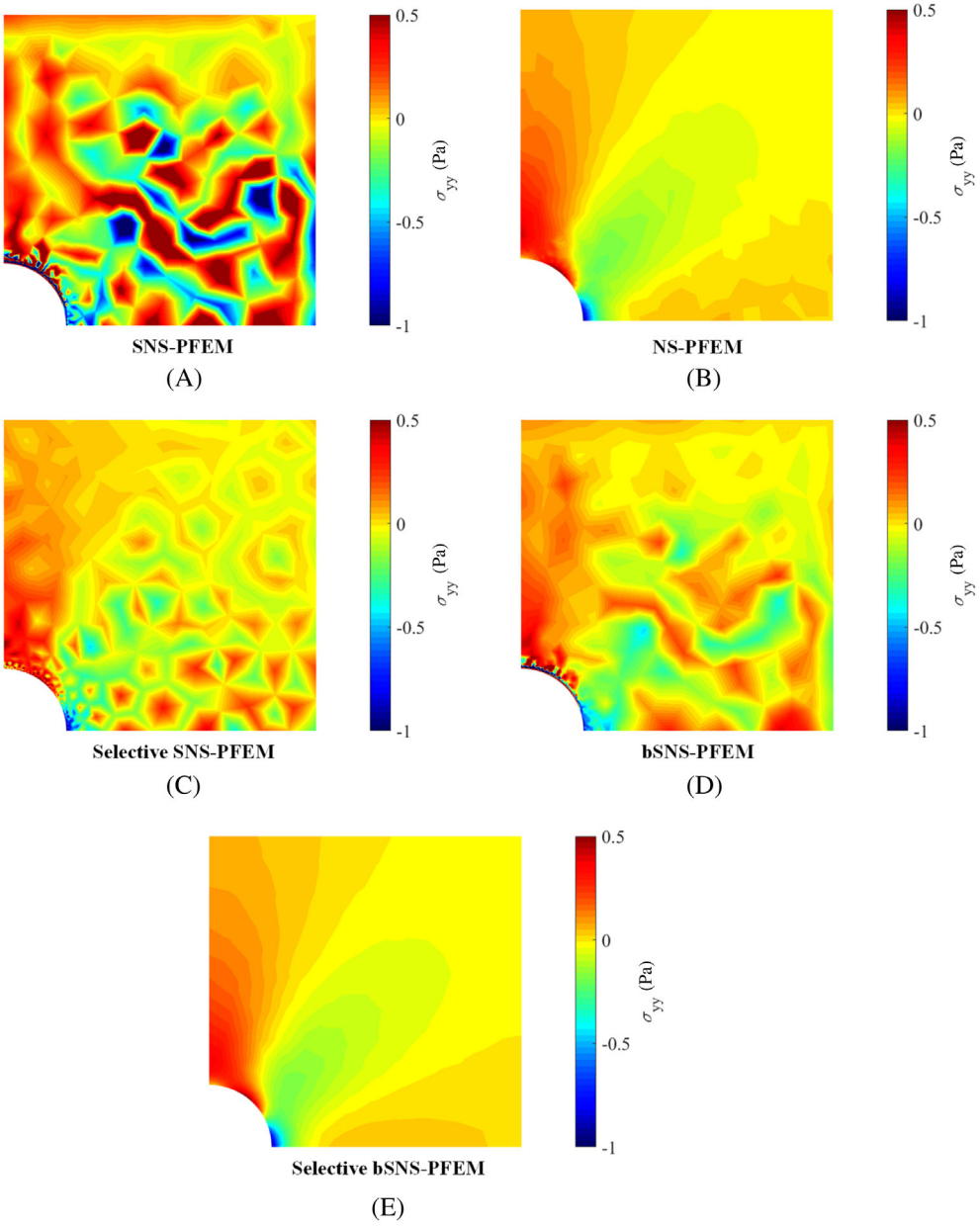

FIGURE 5 Contour of vertical normal stress with different numerical formulations: (A) SNS-PFEM; (B) NS-PFEM; (C) Selective SNS-PFEM; (D) bSNS-PFEM; (E) Selective bSNS-PFEM, of the infinite plate with a circular hole subjected to uniaxial tension ($\upsilon = 0.4999999$)

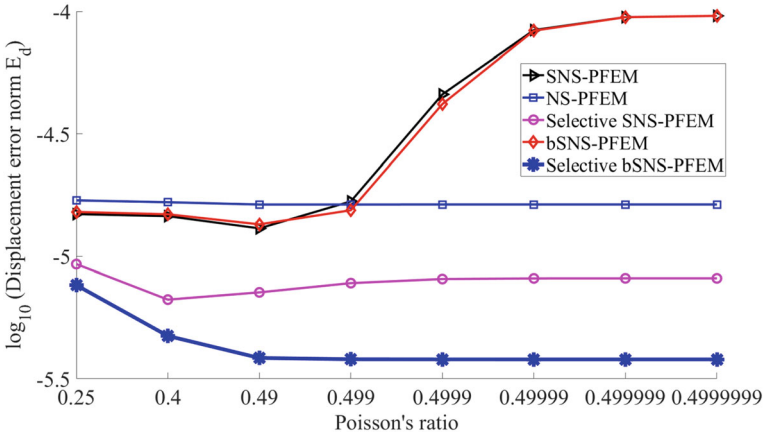

FIGURE 6 Displacement error norm versus Poisson's ratio of the infinite plate with a circular hole subjected to uniaxial tension

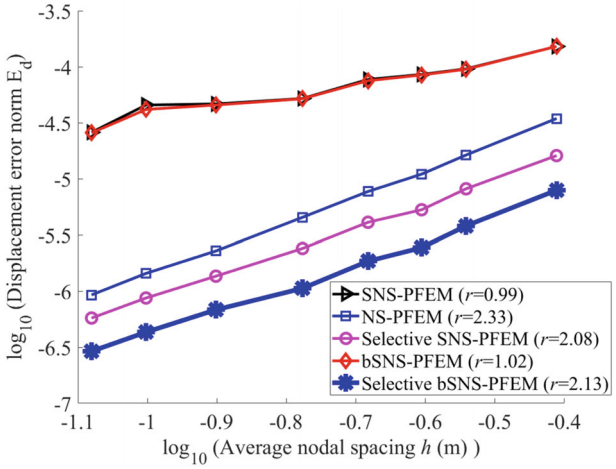

FIGURE 7 Displacement error of the infinite plate with a circular hole subjected to uniaxial tension ($\upsilon = 0.4999999$) using different node densities

bubble function only slightly changes the results. The displacement error of selective SNS-PFEM is even lower than that of NS, but not the lowest. It seems that either the bubble function or selective integration can reduce but not eliminate the locking of SNS-PFEM, while the latter is more effective between them. For selective bSNS-PFEM, the displacement error is stable at the lowest level from 0.49 to the extreme value. The results show that the selective bSNS-PFEM is an effective treatment for nearly incompressible solids. It can preserve the stable nodal integration and locking-free features simultaneously. Besides, the order of magnitude of displacement error norm of selective bSNS-PFEM remains the lowest, between 10^{-5}–10^{-6}, even when the Poisson's ratio is 0.25. It means that it could also be reliably applied to compressible conditions. But this choice is not recommended considering the extra computational cost from the bubble nodes.

Figure 7 presents the convergence of the displacement error of different numerical formulations with the refinement of mesh, where the characteristic size h of discretization is calculated by taking the averaged nodal spacing over all the element edges, and the convergence rate r takes the slope of the fitted lines. The performances of five formulations at the incompressible limit are all improved by mesh refinement more or less. The errors of SNS-PFEM and bSNS-PFEM are close to each other, and the errors of both methods decrease slowly with the convergence rates near 1, even though the mesh is sufficiently refined. The values of displacement error norm of NS-PFEM, selective SNS-PFEM, and selective bSNS-PFEM decrease fast with the convergence rate of more than 2, while the differences among them are always preserved. The NS-PFEM may get close to the locking-free mode at a very fine mesh with the optimal convergence rate of 2.33 among five methods, but the numerical instability due to direct nodal integration still hinders the enhancement of its accuracy. The displacement error of the selective bSNS-PFEM keeps the lowest among these formulations, and also it

preserves a comparative super convergence rate of 2.13 with the NS-PFEM. Overall, it is difficult to reduce the volumetric locking of SNS-PFEM and bSNS-PFEM by merely using more discretization elements. However, refining the mesh can improve the overall performance for NS-PFEM, selective SNS-PFEM and selective bSNS-PFEM.

4.2 | Cook's membrane

The Cook's membrane under combined bending and shear is a well-known benchmark test for volumetric locking[8,10,11,37] since the over stiff feature is very prominent in bending-dominated problems. The plane strain geometry and boundary conditions are described in Figure 8, where the left edge is clamped and the right edge is subjected to a uniformly distributed shear load with an integrated external force of $F = 1$ N. Young's modulus $E = 1$ Pa and the Poisson's ratio is fixed to an extreme value $\upsilon = 0.4999999$. For all the results in Figure 9, a relatively coarse T3 mesh of 139 nodes and 224 elements is used.

Figure 9 depicts the contour of horizontal normal stress on Cook's membrane using different numerical treatments. A similar pattern to that shown in Figure 5 can be observed. The locking-free effect of selective integration scheme is more obvious than that of bubble function, although they are both limited. Only the selective bSNS-PFEM can eliminate both the checkboard locking mode of SNS-PFEM and the spurious oscillatory mode of NS-PFEM to acquire a very smooth solution.

To examine the computational efficiency of different numerical treatments for volumetric locking, the consumed CPU time and the total number of degrees of freedom (DOFs) of the Cook's membrane with a series of mesh densities are presented in Figure 10. The load is linearly applied in 5 steps, and there is 1 iteration per loading step for the elastic problem, which could ensure a fair comparison. All simulations are conducted on the same computer with i7-10750H CPU @ 2.60GHz, 16.0 GB RAM. The PFEM with 6-node quadratic triangular element (T6-PFEM) is also used as a locking-free reference, as shown in Figure 9F. Compared with SNS-PFEM, the methods with bubble nodes could introduce nearly triple the number of DOFs as Figure 10B shows, thus the computational cost rises exponentially. Figure 10A indicates that the difference in CPU time between the SNS-PFEM and selective bSNS-PFEM will be magnified as the mesh is refined. On the other hand, because the number of elements is much less than the number of element edges for the triangular mesh, the computational efficiency of the selective bSNS-PFEM is superior to that of PFEM-T6 for the same mesh. Given the results of Figures 6, 7 and 10, it seems that the selective SNS-PFEM, which does not introduce additional DOF, could be regarded as a cheap alternative to the selective bSNS-PFEM when the numerical model requires a huge number of DOFs, as long as some anticipated accuracy loss is permitted.

4.3 | Stability of an elastoplastic slope

In this section, slope stability analysis under self-weight is conducted with nearly incompressible Tresca and Mohr-Coulomb soil. A sketch of the slope geometry is shown in Figure 11.

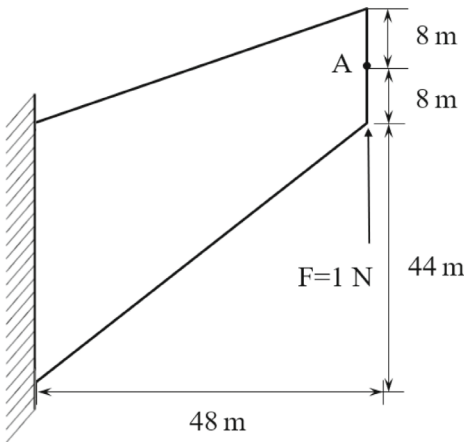

FIGURE 8 Cook's membrane

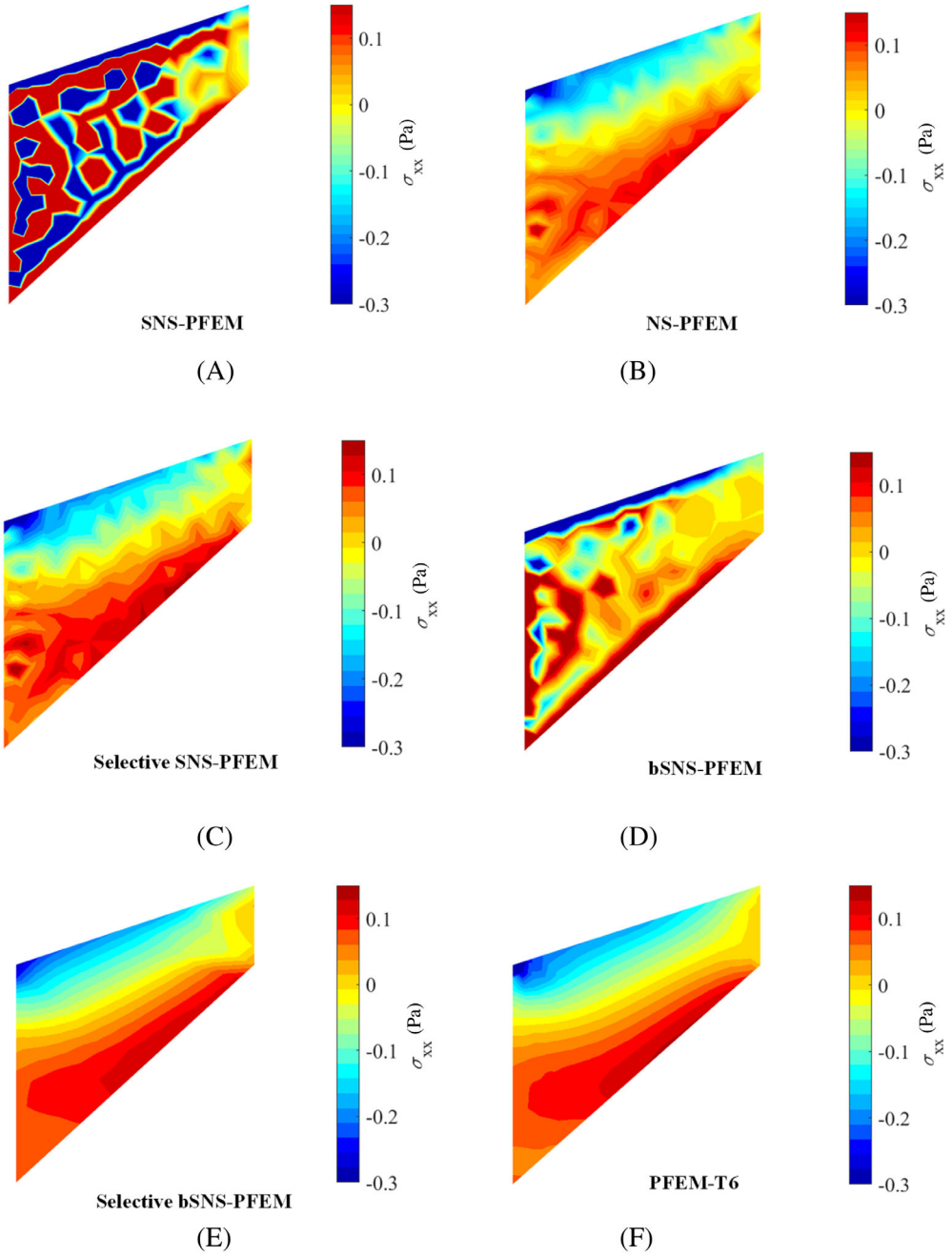

FIGURE 9 Contour of horizontal normal stress with different numerical formulations: (A) SNS-PFEM; (B) NS-PFEM; (C) Selective SNS-PFEM; (D) bSNS-PFEM; (E) Selective bSNS-PFEM; (F) PFEM-T6 of the Cook's membrane

Poisson's ratios between 0.48 to 0.499 are often adopted for undrained saturated soils.[4,48–50] In this section, for Tresca soil: Young's modulus $E = 100$ MPa, Poisson's ratio $\upsilon = 0.499$ and initialized cohesion $c_0 = 25$ kPa. For Mohr-Coulomb soil, Young's modulus $E = 100$ MPa, Poisson's ratio $\upsilon = 0.499$, initialized cohesion $c_0 = 10$ kPa, and frictional angle $\varphi_0 = 20$. The material properties are taken from Zhang et al. and Wang et al.[1,18] The horizontal displacement at the left and right edges and both the horizontal and vertical displacements at the bottom edge are fixed. The soil weight is applied using 20 uniform load steps. The strength reduction factor (SRF) is defined in Equation (30), where $\varphi_0 = 0$ for Tresca soil. A binary procedure is applied to search for the factor of safety (FOS), which is the critical SRF that makes the total number of iterations suddenly increase. Based on the results of the previous two elastic examples, only the SNS-PFEM and selective bSNS-PFEM are implemented and compared in the subsequent elastoplastic analysis.

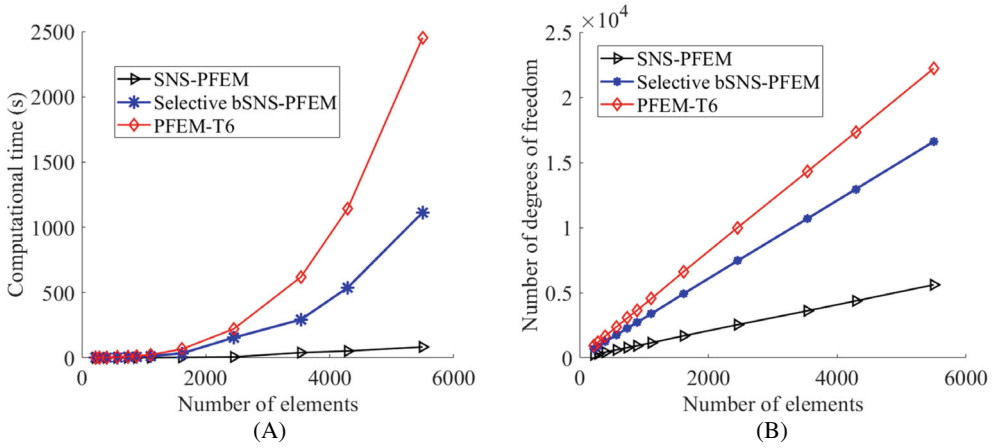

FIGURE 10 Comparison of the (A) computational time and (B) number of degrees of freedom for different locking-free methods with a series of mesh densities

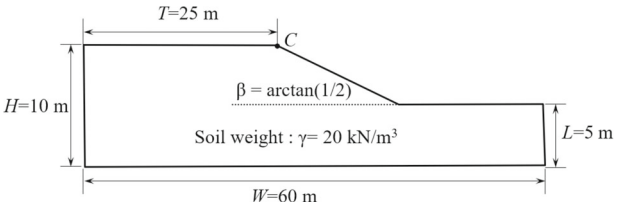

FIGURE 11 Geometry of slope

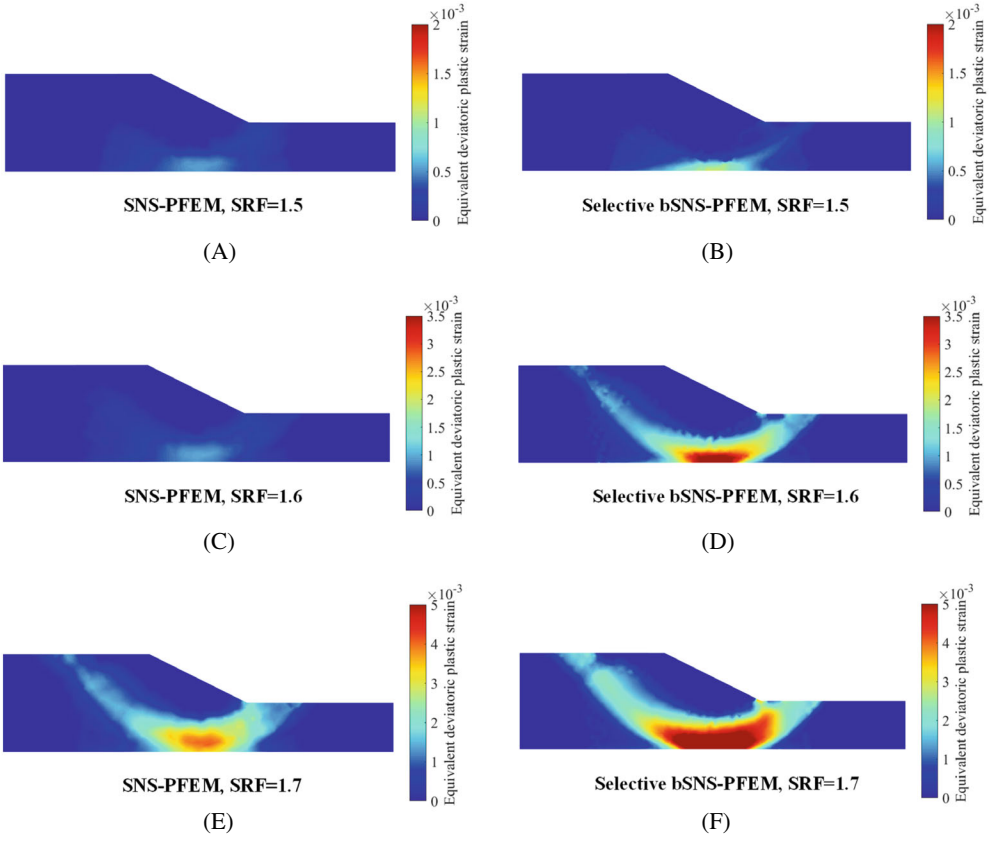

FIGURE 12 Equivalent deviatoric plastic strain of Tresca slope using SNS-PFEM and selective bSNS-PFEM with different strength reduction factors (SRF), $\upsilon = 0.499$

$$\begin{cases} c = \frac{c_0}{SRF}, \\ \varphi = \arctan\left(\frac{\tan\varphi_0}{SRF}\right). \end{cases} \tag{30}$$

Figures 12 and 13 present the equivalent deviatoric plastic strain defined as $\varepsilon_{eq}^{p} = \sqrt{2\left(\mathbf{e}^{p} : \mathbf{e}^{p}\right)/3}$ ($\mathbf{e}^{p}$ is the plastic deviatoric strain tensor) with different SRFs. When the plastic zone just starts to form, the distribution of ε_{eq}^{p} by SNS-PFEM is more oscillatory than that of selective bSNS-PFEM, as shown in Figures 12A,B and 13A,B. When SRF becomes larger, a through slip surface can be acquired with selective bSNS-PFEM, indicating that the FOS has been reached. But this surface is far from forming with SNS-PFEM at the same value of SRF, as depicted in Figures 12C,D and 13C,D. When the SRF is large enough, SNS-PFEM could also give an obvious slip surface, although the equivalent deviatoric plastic strain is lower than that of selective bSNS-PFEM.

The same stability analysis is also conducted with Bishop's method to get reference FOSs. Table 1 shows that for both the Tresca and Mohr-Coulomb slope, the results from selective bSNS-PFEM align well with that of Bishop's method, while SNS-PFEM always gives significantly higher predictions. From Figure 14, the selective bSNS-PFEM always experiences larger displacement than SNS-PFEM since some constraints of volumetric deformation have been removed.

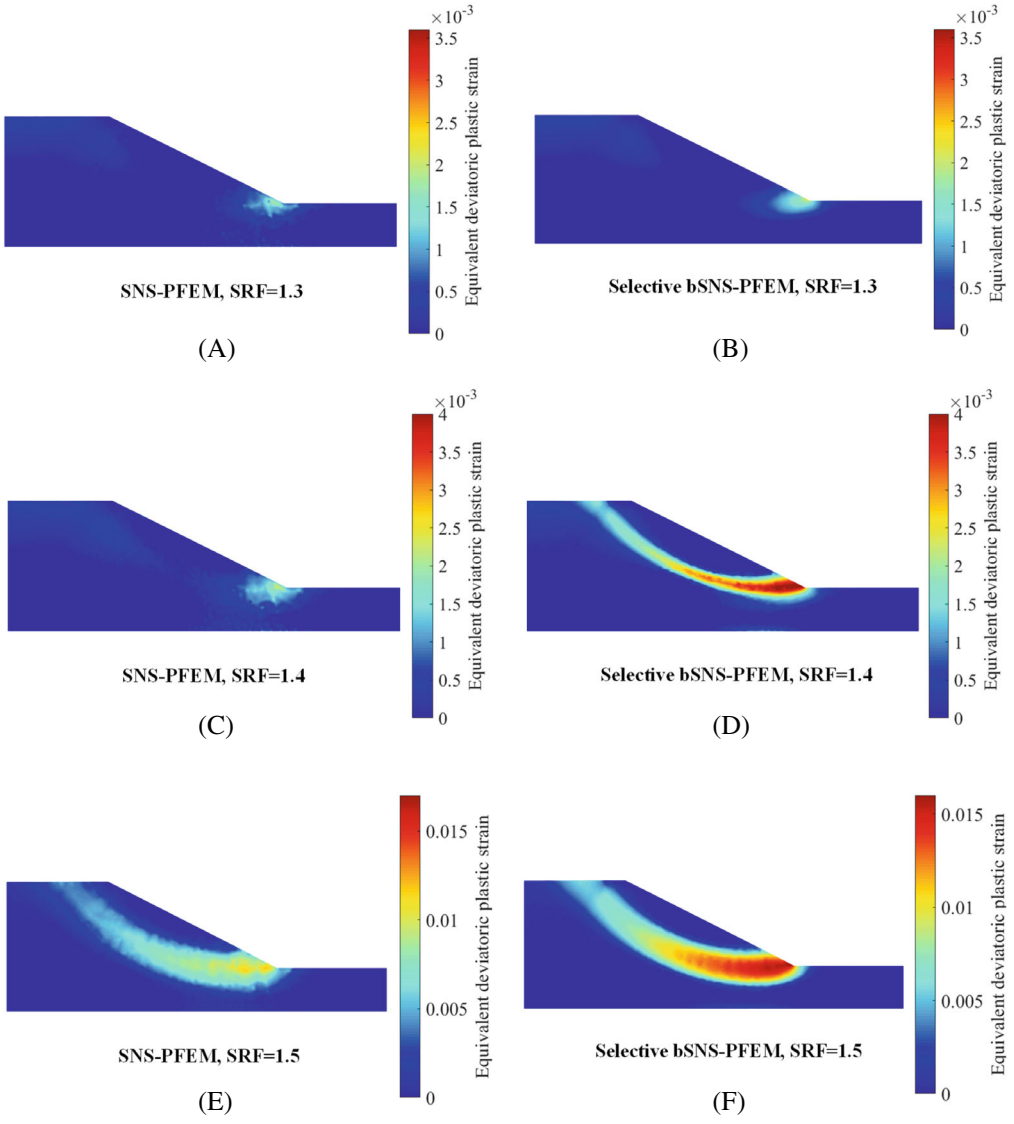

FIGURE 13 Equivalent deviatoric plastic strain of Mohr-Coulomb slope using SNS-PFEM and selective bSNS-PFEM with different strength reduction factors (SRF), $\upsilon = 0.499$

TABLE 1 Factor of safety (FOS) for slope stability analysis

FOS	SNS-PFEM	Selective bSNS-PFEM	Bishop's method
Mohr-Coulomb	1.42	1.38	1.37
Tresca	1.61	1.57	1.57

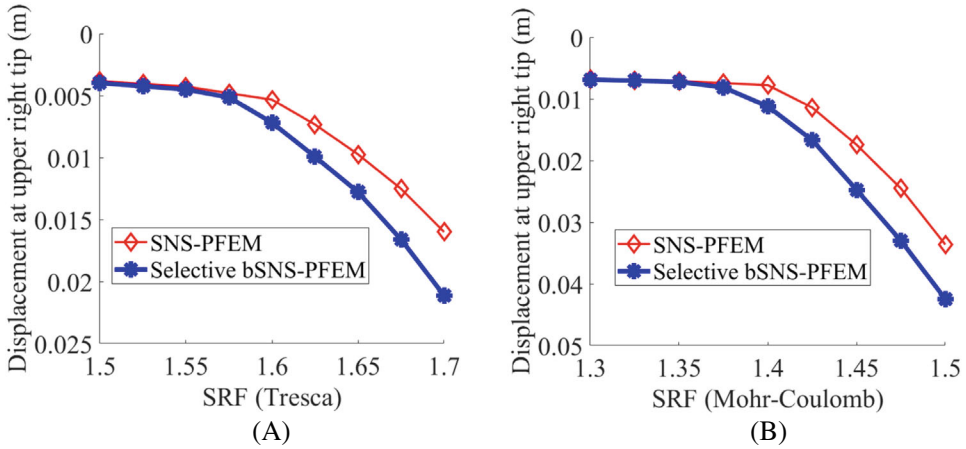

FIGURE 14 Displacement at upper right tip C of slope versus safety reduction factor (SRF) using SNS-PFEM and selective bSNS-PFEM with (A) Tresca soil and (B) Mohr-Coulomb soil

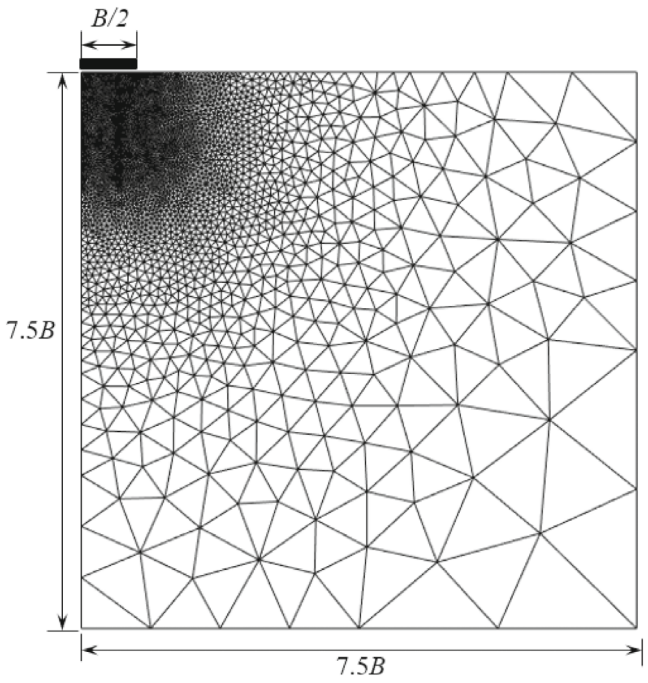

FIGURE 15 Geometry and mesh of strip footing

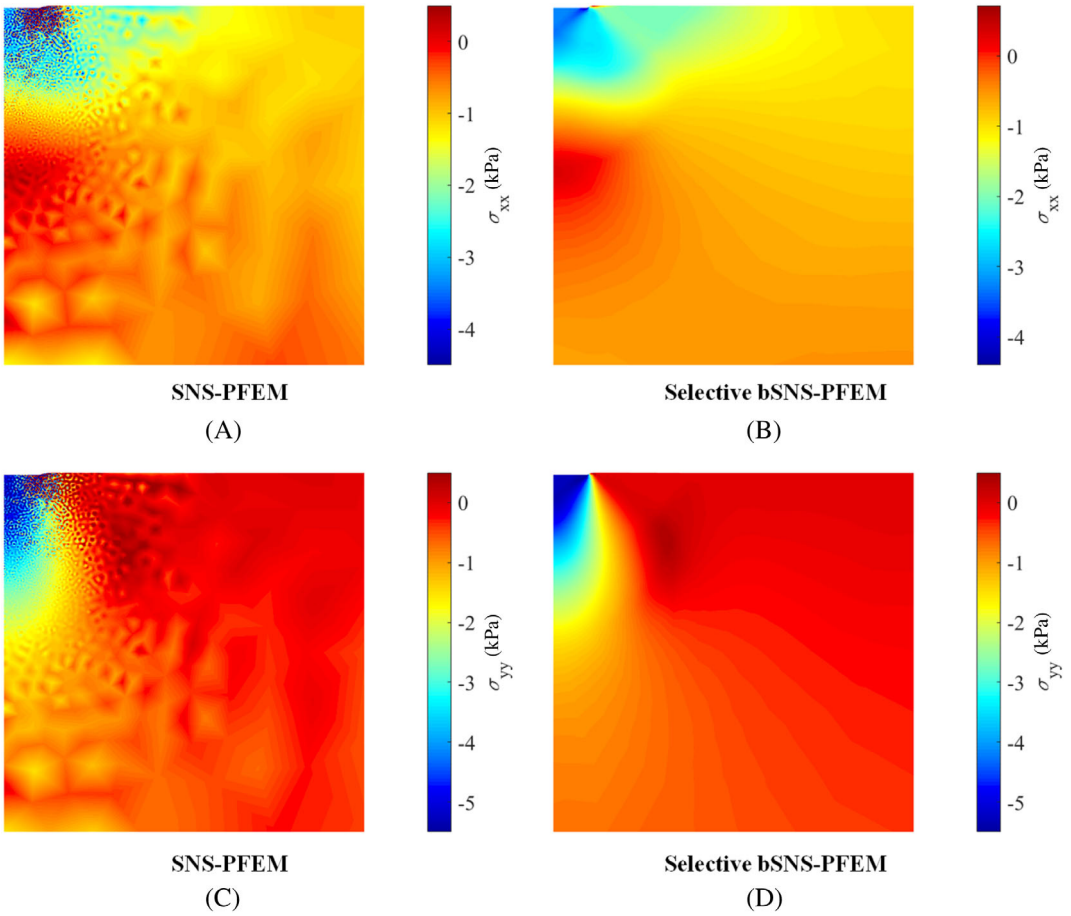

FIGURE 16 Contour of the horizontal and vertical stress of footing penetration problem (small deformation) with SNS-PFEM and Selective bSNS-PFEM, $\upsilon = 0.499$

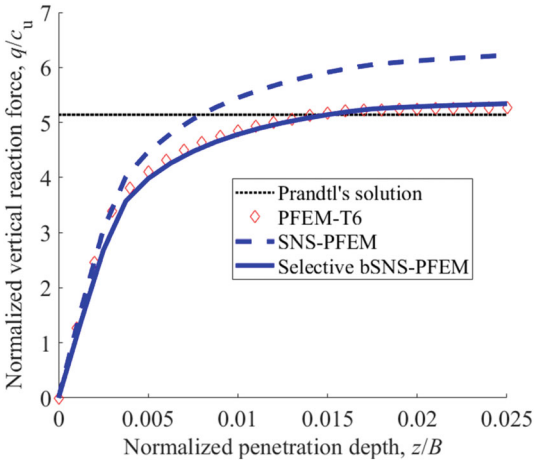

FIGURE 17 Normalized vertical reaction force versus penetration depth for strip footing under small deformation

In the stability analysis of elastoplastic slope, the volumetric locking under nearly incompressible conditions will yield stiffer solutions and an overestimated safety factor, which could bring additional risk to the engineering practice. The locking of SNS-PFEM can be largely decreased by combing the bubble function and selective integration scheme, leading to a more accurate evaluation of FOS.

4.4 | Penetration of a rigid footing on Tresca soil

Rigid footing penetration is a benchmark test of the numerical methods of large deformation.[4,27,48–51] The strong coupling of material and geometric nonlinearity poses a challenge to the accuracy and convergence of prediction as the plastic strain

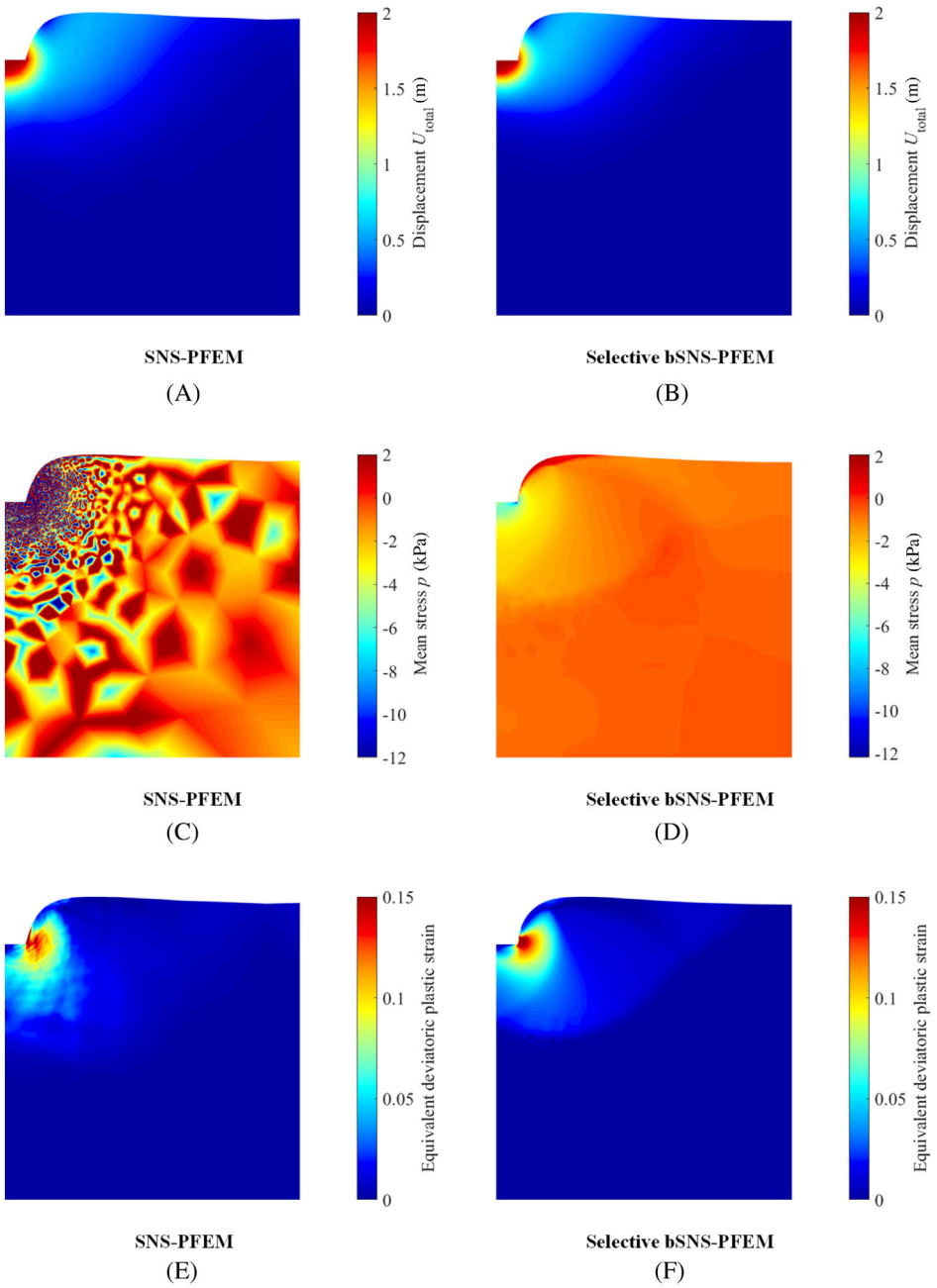

FIGURE 18 Contour of: (A) displacement with SNS-PFEM; (B) displacement with selective bSNS-PFEM; (C) mean stress with SNS-PFEM; (D) mean stress with selective bSNS-PFEM; (E) equivalent deviatoric plastic strain with SNS-PFEM; (F) equivalent deviatoric plastic strain with selective bSNS-PFEM; of footing penetration problem (large deformation), $\upsilon = 0.499$

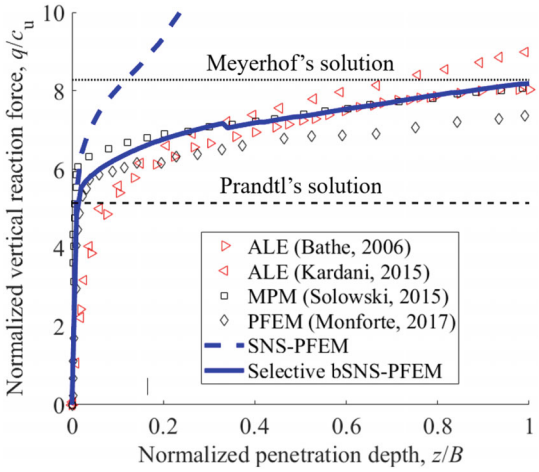

FIGURE 19 Normalized vertical reaction force versus penetration depth for strip footing under large deformation

accumulates. In some previous simulations, the undrained condition of saturated soft soil is approximated by taking a Poisson's ratio of soil near 0.5 to ensure the incremental volumetric strain is small enough.[4,49,50] This approximation tends to introduce volumetric locking in low-order elements, although it may not be so prominent when the Poisson's ratio is around 0.47 or lower. In this example, an extreme value of Poisson's ratio $\upsilon = 0.499$ is adopted. Figure 15 presents the discretized half configuration and mesh with load and boundary conditions, where the half-width of strip footing is set as $B/2 = 1$ m. A nonuniform mesh of 3059 nodes and 5942 elements is used. The weightless soft soil is modeled according to the Tresca model with Young's modulus $E = 100$ kPa and cohesion $c = 1$ kPa. A uniform displacement U is applied at the nodes of the footing bottom by N_S equal steps. For the small deformation analysis, $U = -0.05$ m and $\mathrm{N_S} = 30$. For large deformation analysis, $U = -2$ m and $\mathrm{N_S} = 200$.

In Figure 16, the horizontal and vertical normal stress distribution in small deformation is plotted. The results of SNS-PFEM exhibit the typical checkerboard pattern, while their counterparts of selective bSNS-PFEM are fairly smooth. The normalized vertical reaction force-penetration depth curves are plotted in Figure 17, with Prandtl's solution as the reference.[52] This solution gives the ultimate capacity $(2 + \pi)\, c_u$ of a shallow strip foundation placed on the top of Tresca soil. The curve by selective bSNS-PFEM agrees well with the simulation by PFEM-T6, an element suffering little locking, and tends to be stable at a level near Prandtl's solution. Conversely, the vertical reaction force by SNS-PFEM reaches a significantly higher level due to the overly stiff defect.

Figure 18 presents the contours of total displacement, mean stress and equivalent deviatoric plastic strain when the penetration depth reaches 2 m. It seems that the contour of displacement of SNS-PFEM is only slightly different from that of selective bSNS-PFEM. But the mean stress and equivalent deviatoric plastic strain are severely oscillatory, which can be cured via selective bSNS-PFEM. The normalized vertical reaction force-penetration depth curves are plotted in Figure 19, with Prandtl's solution, Meyerhof's solution and some results from previous studies as references. Meyerhof's solution states that the capacity of a strip foundation deeply embedded in Tresca soil is $(2 + 2\pi)\, c_u$.[53] During the penetration process, the vertical reaction force is believed to go up from Prandtl's solution to Meyerhof's solution, even exceeding the latter if the penetration is deep enough.[51] The vertical reaction force-displacement curves by ALE,[13,49] MPM,[48] and PFEM[4] all fall into the band near the result of selective bSNS-PFEM, with some difference due to the variation of soil properties and features of different numerical methods. However, the vertical reaction force by SNS-PFEM exceeds Meyerhof's solution early on, as the penetration is only around 0.3 m, then rapidly increases to an unpredictable level. The constraint of volumetric deformation of SNS-PFEM seems to be more prominent in large deformation simulations, but this problem can still be effectively solved by the selective bSNS-PFEM.

5 | CONCLUSIONS

This study implemented three novel schemes in the SNS-PFEM: the bubble function to enrich the interpolation space and inject some softening effect (bSNS-PFEM), the selective integration scheme to remove the volumetric constraint in the

incompressible limit (selective SNS-PFEM) and a combination of both (selective bSNS-PFEM) that tries to simultaneously preserve the stable nodal integration and non-locking feature.

The effectiveness and accuracy of the aforementioned schemes were first examined in two elastic examples with a nearly incompressible limit, namely, infinite plate with a circular hole and Cook's membrane. The error analysis with stress contours indicated that introducing the bubble function alone could ease the locking a little, and selective stable integration alone is even more effective, but the checkboard stress pattern still exists. The selective bSNS-PFEM, however, could achieve the best accuracy among all schemes and eliminate the spurious stress oscillations from both unstable nodal integration and volumetric locking. The example of slope stability analysis showed that the selective bSNS-PFEM works well for incompressible Tresca and Mohr-Coulomb materials, giving similar predictions of FOS in Bishop's method. The footing penetration case indicated that volumetric locking would be more severe under large deformation with SNS-PFEM, whereas the selective bSNS-PFEM still works well.

The most obvious shortcoming of the proposed selective bSNS-PFEM is the prominent increase of computational cost due to extra degrees of freedom from bubble nodes, as Figure 10 shows, although it is easily implemented into S-PFEM codes. Therefore, the formulation of selective bSNS-PFEM is best regarded as a specifically designed version for nearly incompressible problems, and it is also reliable under compressible conditions, as supported by the error analysis of the infinite plate with a circular hole when the Poisson's ratio is 0.25. Besides, this study is restricted to the applications of pure-solid problems with plane-strain SNS-PFEM. Future work will focus on the improvement of selective bubble-SNS-PFEM in two aspects. One is the 3D extension of the current method. A similar low-order interpolation scheme using the 4-node linear tetrahedron element (T4) could be adopted. As both the elements are simplices, it can be anticipated that most of the numerical features in this article can be preserved in the 3D condition. Another aspect is to investigate the performance of the proposed locking-free methods in more complicated nearly incompressible conditions in geotechnical practice,[54] such as the coupled hydro-mechanical analysis.

ACKNOWLEDGMENTS

This research is financially supported by the Hong Kong Polytechnic University Strategic Importance Fund (ZE2T) and Project of Research Institute of Land and Space (CD78), and the Research Grants Council (RGC) of Hong Kong Special Administrative Region Government (HKSARG) of China (Grant No. R5037-18F).

CONFLICT OF INTEREST

We declare that we have no known competing financial interests or personal relationships that could have appeared to influence the work reported in this article.

DATA AVAILABILITY STATEMENT

The data that support the findings of this study are available from the corresponding author upon reasonable request.

ORCID

Ze-Yu Wang https://orcid.org/0000-0001-8130-9672
Yin-Fu Jin https://orcid.org/0000-0003-0522-1702
Zhen-Yu Yin https://orcid.org/0000-0003-4154-7304
Yu-Ze Wang https://orcid.org/0000-0003-3085-5299

REFERENCES

1. Wang L, Zhang X, Tinti S. Large deformation dynamic analysis of progressive failure in layered clayey slopes under seismic loading using the particle finite element method. *Acta Geotech*. 2021;16(8):2435-2448.
2. Monforte L, Arroyo M, Carbonell JM, Gens A. Coupled effective stress analysis of insertion problems in geotechnics with the particle finite element method. *Comput Geotech*. 2018;101:114-129.
3. Monforte L, Carbonell JM, Arroyo M, Gens A. Performance of mixed formulations for the particle finite element method in soil mechanics problems. *Comput Part Mech*. 2017;4(3):269-284.
4. Monforte L, Arroyo M, Carbonell JM, Gens A. Numerical simulation of undrained insertion problems in geotechnical engineering with the particle finite element method (PFEM). *Comput Geotech*. 2017;82:144-156.
5. Zhang X, Krabbenhoft K, Sheng DC, Li WC. Numerical simulation of a flow-like landslide using the particle finite element method. *Comput Mech*. 2015;55(1):167-177.
6. Zhang X, Krabbenhoft K, Sheng DC. Particle finite element analysis of the granular column collapse problem. *Granular Matter*. 2014;16(4):609-619.

7. Coombs WM, Charlton TJ, Cortis M, Augarde CE. Overcoming volumetric locking in material point methods. *Comput Method Appl M*. 2018;333:1-21.
8. Ortiz-Bernardin A, Hale JS, Cyron CJ. Volume-averaged nodal projection method for nearly-incompressible elasticity using meshfree and bubble basis functions. *Comput Methods Appl Mech Eng*. 2015;285:427-451.
9. Belytschko T, Liu WK, Moran B, Elkhodary K. *Nonlinear Finite Elements for Continua and Structures*. John wiley & sons; 2013.
10. de Souza Neto EA, Pires FMA, Owen DRJ. F-bar-based linear triangles and tetrahedra for finite strain analysis of nearly incompressible solids. Part I: formulation and benchmarking. *Int J Numer Methods Eng*. 2005;62(3):353-383.
11. Nguyen-Xuan H, Liu GR. An edge-based smoothed finite element method softened with a bubble function (bES-FEM) for solid mechanics problems. *Comput Struct*. 2013;128:14-30.
12. Hughes TJ. *The Finite Element Method: Linear Static and Dynamic Finite Element Analysis*. Courier Corporation; 2012.
13. Bathe K-J. *Finite Element Procedures*. Prentice-Hall; 1996.
14. Liu GR, Nguyen-Thoi T, Nguyen-Xuan H, Lam KY. A node-based smoothed finite element method (NS-FEM) for upper bound solution to solid mechanics problems. *Comput Struct*. 2009;87(1–2):14-26.
15. Guo N, Yang ZX, Yuan WH, Zhao JD. A coupled SPFEM/DEM approach for multiscale modeling of large-deformation geomechanical problems. *Int J Numer Anal Methods Geomech*. 2021;45(5):648-667.
16. Yuan WH, Liu K, Zhang W, Dai BB, Wang Y. Dynamic modeling of large deformation slope failure using smoothed particle finite element method. *Landslides*. 2020;17(7):1591-1603.
17. Yuan WH, Wang B, Zhang W, Jiang Q, Feng XT. Development of an explicit smoothed particle finite element method for geotechnical applications. *Comput Geotech*. 2019;106:42-51.
18. Zhang W, Yuan WH, Dai BB. Smoothed particle finite-element method for large-deformation problems in Geomechanics. *Int J Geomech*. 2018;18(4):04018010.
19. Zhang W, Zhong ZH, Peng C, Yuan WH, Wu W. GPU-accelerated smoothed particle finite element method for large deformation analysis in geomechanics. *Comput Geotech*. 2021;129:103856.
20. Jin YF, Yin ZY, Yuan WH. Simulating retrogressive slope failure using two different smoothed particle finite element methods: a comparative study. *Eng Geol*. 2020;279:105870.
21. Jin YF, Yuan WH, Yin ZY, Cheng YM. An edge-based strain smoothing particle finite element method for large deformation problems in geotechnical engineering. *Int J Numer Anal Methods Geomech*. 2020;44(7):923-941.
22. Li Y, Liu GR. A novel node-based smoothed finite element method with linear strain fields for static, free and forced vibration analyses of solids. *Appl Math Comput*. 2019;352:30-58.
23. Zeng W, Liu GR. Smoothed finite element methods (S-FEM): an Overview and recent developments. *Arch Comput Methods Eng*. 2018;25(2):397-435.
24. Liu GR, Nguyen-Thoi T, Lam KY. An edge-based smoothed finite element method (ES-FEM) for static, free and forced vibration analyses of solids. *J Sound Vib*. 2009;320(4):1100-1130.
25. Cremonesi M, Franci A, Idelsohn S, Onate E. A state of the art review of the particle finite element method (PFEM). *Arch Comput Methods Eng*. 2020;27(5):1709-1735.
26. Onate E, Idelsohn SR, Del Pin F, Aubry R. The particle finite element method - an overview. *Int J Comp Methods*. 2004;1(2):267-307.
27. Jin YF, Yin ZY, Zhou XW, Liu FT. A stable node-based smoothed PFEM for solving geotechnical large deformation 2D problems. *Comput Methods Appl Mech Eng*. 2021;387:114179.
28. Jiang C, Han X, Liu GR, Zhang ZQ, Yang G, Gao GJ. Smoothed finite element methods (S-FEMs) with polynomial pressure projection (P3) for incompressible solids. *Eng Anal Bound Elem*. 2017;84:253-269.
29. Puso MA, Chen JS, Zywicz E, Elmer W. Meshfree and finite element nodal integration methods. *Int J Numer Methods Eng*. 2008;74(3):416-446.
30. Chen JS, Wu CT, Yoon S, You Y. A stabilized conforming nodal integration for Galerkin meshfree methods. *Int J Numer Methods Eng*. 2001;50(2):435-466.
31. Jin Y-F, Yin Z-Y. Two-phase PFEM with stable nodal integration for large deformation hydromechanical coupled geotechnical problems. *Comput Methods Appl Mech Eng*. 2022;392:114660.
32. Shafee A, Khoshghalb A. An improved node-based smoothed point interpolation method for coupled hydro-mechanical problems in geomechanics. *Comput Geotech*. 2021;139:104415.
33. Yang H, Cui XY, Li S, Bie YH. A stable node-based smoothed finite element method for metal forming analysis. *Comput Mech*. 2019;63(6):1147-1164.
34. Hillman M, Chen JS. An accelerated, convergent, and stable nodal integration in Galerkin meshfree methods for linear and nonlinear mechanics. *Int J Numer Methods Eng*. 2016;107(7):603-630.
35. Feng H, Cui XY, Li GY. A stable nodal integration method with strain gradient for static and dynamic analysis of solid mechanics. *Eng Anal Bound Elem*. 2016;62:78-92.
36. Sussman T, Bathe KJ. A finite-element formulation for nonlinear incompressible elastic and inelastic analysis. *Comput Struct*. 1987;26(1–2):357-409.
37. Moutsanidis G, Koester JJ, Tupek MR, Chen JS, Bazilevs Y. Treatment of near-incompressibility in meshfree and immersed-particle methods. *Comput Part Mech*. 2020;7(2):309-327.
38. Navas P, Lopez-Querol S, Yu RC, Pastor M. Optimal transportation meshfree method in geotechnical engineering problems under large deformation regime. *Int J Numer Methods Eng*. 2018;115(10):1217-1240.

39. Bower AF. *Applied Mechanics of Solids*. CRC Press; 2009.
40. Nguyen TT, Liu GR, Dai KY, Lam KY. Selective smoothed finite element method. *Tsinghua Sci Technol*. 2007;12(5):497-508.
41. Cardoso RPR, Yoon JW, Mahardika M, Choudhry S, de Sousa RJA, Valente RAF. Enhanced assumed strain (EAS) and assumed natural strain (ANS) methods for one-point quadrature solid-shell elements. *Int J Numer Methods Eng*. 2008;75(2):156-187.
42. Simo JC, Rifai MS. A class of mixed assumed strain methods and the method of incompatible modes. *Int J Numer Methods Eng*. 1990;29(8):1595-1638.
43. Simo JC, Taylor RL, Pister KS. Variational and projection methods for the volume constraint in finite deformation elasto-plasticity. *Comput Methods Appl Mech Eng*. 1985;51(1–3):177-208.
44. Lamichhane BP. Inf-sup stable finite-element pairs based on dual meshes and bases for nearly incompressible elasticity. *Ima J Numer Anal*. 2009;29(2):404-420.
45. Arnold DN, Brezzi F, Fortin MJC. A stable finite element for the stokes equations. *Calcolo*. 1984;21(4):337-344.
46. Wei HY, Chen JS, Hillman M. A stabilized nodally integrated meshfree formulation for fully coupled hydro-mechanical analysis of fluid-saturated porous media. *Comput Fluids*. 2016;141:105-115.
47. Liu G-R, Quek SS. *The Finite Element Method: A Practical Course*. Butterworth-Heinemann; 2013.
48. Solowski WT, Sloan SW. Evaluation of material point method for use in geotechnics. *Int J Numer Anal Methods Geomech*. 2015;39(7):685-701.
49. Kardani M, Nazem M, Carter JP, Abbo AJ. Efficiency of high-order elements in large-deformation problems of Geomechanics. *Int J Geomech*. 2015;15(6):04014101.
50. Nazem M, Sheng DC, Carter JP. Stress integration and mesh refinement for large deformation in geomechanics. *Int J Numer Methods Eng*. 2006;65(7):1002-1027.
51. da Silva MV, Krabbenhoft K, Lyamin AV, Sloan SW. Rigid-plastic large-deformation analysis of geotechnical penetration problems. University of New South Wales (UNSW), Centre for Infrastructure Engineering and Safety (CIES); 2011.
52. Prandtl L. Hauptaufsätze: Über die Eindringungsfestigkeit (Härte) plastischer Baustoffe und die Festigkeit von Schneiden. *J Appl Math Mech*. 1921;1(1):15-20.
53. Meyerhof G. The ultimate bearing capacity of foudations. *Geotechnique*. 1951;2(4):301-332.
54. Zhang Q, Yan X, Li ZH. A mathematical framework for multiphase poromechanics in multiple porosity media. *Comput Geotech*. 2022;146:104728.

How to cite this article: Wang Z-Y, Jin Y-F, Yin Z-Y, Wang Y-Z. Overcoming volumetric locking in stable node-based smoothed particle finite element method with cubic bubble function and selective integration. *Int J Numer Methods Eng*. 2022;1-22. doi: 10.1002/nme.7107

APPENDIX A. SMOOTHED GRADIENT MATRIX

The idea of node-based smoothed gradient comes from the stabilized conforming nodal integration.[30] The formulations of calculating smoothed gradient matrix $\overline{\mathbf{B}}$ is exhibited as follows. The subdomain-smoothed matrix $\overline{\mathbf{B}}^{sub}$ can be calculated in the same way, just replacing the integration domain. By applying the divergence theorem, the smoothing operator can be transformed into contour integration of shape function along the boundary of smoothing domain as in Equations (A1) and (A2)

$$\begin{aligned}\overline{\mathbf{B}}_I(\mathbf{x})\Big|_{\Omega_k^s} &= \int_{\Omega_k^s} \mathbf{B}_I(\mathbf{x})\widehat{W}(\mathbf{x}_k - \mathbf{x})\, d\mathbf{x} \\ &= \frac{1}{A_k^s}\int_{\Omega_k^s} \mathbf{L}_d \mathbf{N}_I(\mathbf{x}) d\mathbf{x} \\ &= \frac{1}{A_k^s}\int_{\Gamma_k^s} \mathbf{L}_n \mathbf{N}_I(\mathbf{x}) d\mathbf{x}, \end{aligned} \tag{A1}$$

$$\mathbf{L}_n = \begin{bmatrix} n_x & 0 \\ 0 & n_y \\ n_y & n_x \end{bmatrix}, \tag{A2}$$

where n_x and n_y are two components of the outer normal unit vector $\mathbf{n}$ as in Figure 1.

Noticing that the boundary of smoothing domain is composed of segmented lines, the Gaussian integration of each term of $\overline{\mathbf{B}}_I$ could be conducted using the formulation presented in Equation (A3)

$$\int_{\Gamma_k^s} N_I(\mathbf{x}) n_a(\mathbf{x}) d\Gamma = \sum_{seg=1}^{M} n_{a,seg} l_{seg} \sum_{i=1}^{G} N_I\left(x_{seg,i}^{GP}\right) w_i, \quad a \in \{x, y\}, \tag{A3}$$

where M is the number of boundary segments and G is the order of Gaussian integration. $G \geq 2$ when the required integrand order is greater than one, that is, the gradients of cubic bubble function.

APPENDIX B. COMPUTATIONAL CYCLE OF SNS-PFEM

The computational cycle of SNS-PFEM is summarized as follows.

1. Initialize the geometry and all given parameters.
2. Discretize the domain into a cloud of nodes (particles).
3. Form the mesh using Delaunay triangulation, and number the degrees of freedom including bubble nodes if needed.
4. Assemble the smoothed stiffness matrix with selective stable nodal integration and apply all the boundary conditions.
5. Solve the nonlinear S-FEM equations in a single load step using Newton–Raphson or initial stiffness iteration scheme until the convergence criterion is satisfied.
6. Update the positions of nodes and renew all the physical quantities of interest.
7. Rebuild the mesh (and internal bubble nodes if needed) with Delaunay triangulation and alpha shape method. Then go back to step 4 until all the calculation steps are finished.